


## Understanding Complex Magnetic Spin Textures with Simulation-Assisted Lorentz Transmission Electron Microscopy

Arthur R.C. McCray<sup>1,2,\*</sup> Timothy Cote<sup>1,3</sup> Yue Li<sup>1</sup> Amanda K. Petford-Long<sup>1,3</sup> and Charudatta Phatak<sup>1,†</sup>

<sup>1</sup>Materials Science Division, Argonne National Laboratory, Lemont, Illinois 60439, USA

<sup>2</sup>Applied Physics Program, Northwestern University, Evanston, Illinois 60208, USA

<sup>3</sup>Department of Materials Science and Engineering, Northwestern University, Evanston, Illinois 60208, USA

 (Received 5 January 2021; revised 18 March 2021; accepted 24 March 2021; published 14 April 2021)

There is an increased interest in topologically nontrivial magnetic spin textures such as skyrmions and chiral domain-wall solitons, both from a point of fundamental physics understanding as well as potential technological interest in low-power memory applications. In order to control their behavior, it is necessary to understand their complex spin texture at the nanoscale. Lorentz transmission electron microscopy (LTEM) is a suitable technique for studying these systems due to its high spatial resolution and capability to simultaneously characterize magnetic texture and microstructure. In this work, we present the application of PyLorentz, an open-source software suite that we have developed, for quantitative image analysis of Néel-type skyrmions in thin-film heterostructures. PyLorentz enhances LTEM capabilities by enabling reconstruction of magnetic induction maps from experimental images, as well as simulating LTEM images using micromagnetic simulation data. We demonstrate this for simulated Néel skyrmions as well as experimental data from [Pt/Co/W] multilayer heterostructures. We also show how simulation-assisted LTEM analysis is crucial for understanding these complex magnetic spin textures, in which the reconstructed magnetic induction map (seen in the LTEM images) differs significantly from the magnetization configuration.

DOI: [10.1103/PhysRevApplied.15.044025](https://doi.org/10.1103/PhysRevApplied.15.044025)

### I. INTRODUCTION

Magnetic spin textures on the micro- and nanoscale are of growing interest due to the complex topological states they can exhibit [1,2]. Understanding these magnetic textures gives insights into fundamental physical phenomena that can potentially be harnessed for technological applications. Skyrmions, for example, are candidates for next-generation information carriers as a result of their stability and high mobility in response to an electric current. These properties arise from their three-dimensional winding topology [3], meaning that their magnetization cannot be reduced to a uniform state without overcoming a finite energy barrier. Skyrmions are most commonly stabilized by the Dzyaloshinskii-Moriya interaction (DMI), a chiral energy term arising from inversion-symmetry breaking [4,5]. In multilayer films, the competing DMI, exchange, and anisotropy energies can create skyrmion lattices in ordered arrays that could be developed for efficient memory uses [6,7]. Increasing attention is also being turned to magnetic textures with higher topological charge such as target skyrmions and hopfions [8,9]. Understanding the

energy landscape of such magnetic nanostructures is necessary to determine the governing energy terms, especially in cases where there are several competing energies. Furthermore, to control the magnetic properties, it is necessary not only to understand the local variations in magnetization at the nanoscale, but also to correlate them with the microstructure and composition. For example, structural defects can strongly influence the behavior of magnetic domains [10].

There are several aspects to characterizing materials that contain nanomagnetic spin textures, and Lorentz transmission electron microscopy (LTEM) is especially well suited to the task. Firstly, high-resolution characterization of the magnetization is necessary as a useful aspect of skyrmions and other potential spin textures for information storage technologies is their high spatial density and small size, which can be less than 10 nm in diameter [1]. Secondly, LTEM enables simultaneous characterization of microstructure and microstructural defects that can be correlated with magnetic domain behavior, particularly during *in situ* experiments as a function of external stimuli such as temperature, and electric or magnetic fields.

The magnetic contrast in LTEM images depends on the interaction between the transmitted electrons and the

\*arthurmccray@u.northwestern.edu

†cd@anl.gov

components of the local magnetic induction perpendicular to their direction of propagation [11–14]. Out-of-focus imaging in a transmission electron microscope produces Fresnel contrast, wherein magnetic domain walls appear as bright or dark lines relative to the domains themselves. Although such images are easy to interpret for simple magnetic domain structures, analysis of complex magnetic textures requires quantitative magnetic information. Such information is carried by the phase of the electron wave, and can be retrieved experimentally using various methods such as off-axis holography, four-dimensional (4D) scanning (S)TEM techniques, and the transport-of-intensity equation (TIE). Off-axis holography has long been used for phase retrieval [15], but requires a special experimental setup including an electrostatic biprism and also suffers from a limited field of view. 4D-STEM techniques offer the highest resolution, but they rely on pixelated detectors that are not easily accessible and intensive data acquisition and analysis [16]. The TIE method, meanwhile, is straightforward to implement and requires only a through-focal series of images for phase reconstruction [11]. However, it requires solving a partial differential equation, and hence appropriate boundary conditions, and accurate image alignment.

Here we present a quantitative analysis of Néel-type skyrmions using simulation-assisted LTEM enabled by PyLorentz. We have developed PyLorentz [17] as a comprehensive open-source software suite to enable quantitative mapping of magnetic induction using TIE reconstruction as well as simulating LTEM images under realistic microscope conditions from micromagnetic simulation output. Matching simulated and experimental images can provide further information about the sample by providing quantitative information about the energy landscape and allowing us to separate out the intrinsic magnetization texture and the stray fields, both of which contribute to the LTEM images.

Topologically nontrivial magnetic spin textures are often three dimensional (3D) and must therefore be imaged in three dimensions, for example, at different sample tilts, to be fully understood. To this end, we have developed a method in PyLorentz for calculating the phase shift of 3D objects with complex magnetization, allowing LTEM image simulations of 3D magnetic textures at any orientation. We demonstrate the application of this approach to simulating the phase shift and corresponding LTEM images of Néel-type magnetic skyrmions at various sample tilts. We also show the usefulness of knowing the microscope parameters when interpreting Fresnel contrast in LTEM images. Finally, we show the reconstruction of magnetic induction maps for experimental data from multilayer heterostructure thin films of  $[\text{Pt}/\text{Co}/\text{W}]_n$  that exhibit Néel-type skyrmions, and we comment on the accurate interpretation of such maps.

## II. RESULTS

The basic workflow for PyLorentz is shown in Fig. 1. All the functions within the blue box are written entirely in Python for easy implementation and are publicly available on GitHub. The input for PyLorentz can be either 3D magnetization data from micromagnetic simulations, such as output from OOMMF [18] or MuMax [19], or experimentally collected LTEM images on which to perform TIE phase reconstruction directly. For the former, in order to simulate the LTEM images, we need to compute the phase shift imparted to the electron waves after their interaction with the sample, given by the Aharonov-Bohm relation [20]. This includes determining the contributions from the magnetic vector potential as well as the electrostatic potential.

Accurate calculation of the total phase shift is the critical and most difficult step in simulating LTEM images of magnetic samples with complex magnetic spin textures. We develop a method for calculating this phase shift for an arbitrary magnetization configuration, using the linear superposition principle that is described in Sec. II A. Once the phase shift is calculated, we can compute the electron exit wave function, which is then convolved with the microscope transfer function to obtain the image wave function.

Relevant electron microscope parameters such as defocus, spherical aberration, astigmatism, and beam coherence can be set by the user to define the microscope transfer function. The resulting LTEM images are simulated from the calculated phase shift and the transfer function as described in the appendix. The final step, which is the TIE formalism, can then be applied to these images, or to aligned experimental data, to reconstruct the phase shift and the integrated magnetic induction maps. PyLorentz supports phase retrieval in three different modes: (i) separation of magnetic and electrostatic phase shifts when provided with both a through-focal series of the sample as is and inverted by  $180^\circ$ ; (ii) total phase shift when only a single through-focal series is available; and (iii) single defocus image-based phase retrieval [21] as described in Sec. II C.

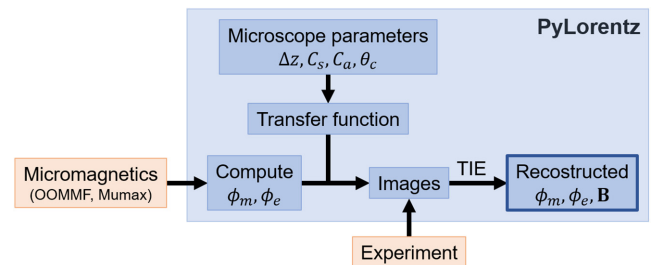


FIG. 1. PyLorentz workflow from input experimental images or micromagnetic simulation data to the reconstructed phase shifts and integrated induction maps.

### A. Calculating electron phase shifts

PyLorentz includes a forward-model-based algorithm for calculating the electron phase shift as a result of passing through a magnetic material. The most commonly used method for this calculation is based on the Mansuripur algorithm [22,23], which finds the components of the magnetic vector potential for thin films with a magnetization that is uniform along the direction normal to the film. The Mansuripur method is based on a direct Fourier transform of the magnetization and is very efficient, but for tomography and for magnetic structures that vary along the beam direction, a different approach is needed.

To that end we develop a method to calculate the phase shift based on representing the 3D magnetic spin texture using the linear superposition of a magnetic dipole at each voxel. This algorithm can calculate electron phase shifts through samples of any geometry and at any tilt angle within the microscope. This is helpful as many magnetic samples require being tilted in the microscope, either to view spin textures that do not produce contrast when viewed in plane [24] or to distinguish magnetization distributions that vary along the  $z$  axis [1,25].

In Lorentz TEM, the information about the magnetization distribution of the sample is carried by the phase of the electron wave. The Aharonov-Bohm expression [20] describes the interaction of an electron with an electrostatic potential  $V(\mathbf{r})$  and a magnetic vector potential  $\mathbf{A}(\mathbf{r})$ . These two components contribute to the total phase shift ( $\phi_t$ ) as

$$\begin{aligned}\phi_t(\mathbf{r}_\perp) &= \phi_e(\mathbf{r}_\perp) + \phi_m(\mathbf{r}_\perp), \\ &= \frac{\pi}{\lambda E} \int V(\mathbf{r}_\perp) d\mathbf{l} - \frac{\pi}{\phi_0} \int \mathbf{A}(\mathbf{r}_\perp) \cdot d\mathbf{l},\end{aligned}\quad (1)$$

where  $\lambda$  is the electron wavelength,  $E$  the relativistic electron energy,  $\mathbf{r}_\perp$  the two-dimensional (2D) position vector in the projected plane perpendicular to the electron propagation direction  $\mathbf{l}$ , and  $\phi_0 = h/2e$  is the magnetic flux quantum.  $\phi_m$  and  $\phi_e$  are the magnetic and electrostatic components of the total electron phase shift  $\phi_t$ . We primarily focus on  $\phi_m$  in the discussion in this section. We define our coordinate system as having  $x$  and  $y$  within the plane perpendicular to the electron beam and  $z$  pointing opposite to the direction of electron propagation. We treat this as the lab or microscope reference frame, within which the magnetic sample (object) can be tilted.

The vector potential can be written as a convolution of the magnetization  $\mathbf{M}(\mathbf{r})$ :

$$\mathbf{A}(\mathbf{r}) = \frac{\mu_0}{4\pi} \int \mathbf{M}(\mathbf{r}') \times \frac{\mathbf{r} - \mathbf{r}'}{|\mathbf{r} - \mathbf{r}'|^3} d^3\mathbf{r}'.\quad (2)$$

This relation can be expressed in a simpler form using a Fourier transform and the linearity of the vector product

operation to write

$$\mathbf{A}(\mathbf{k}) = -\frac{i\mu_0}{k^2} \mathbf{M}(\mathbf{k}) \times \mathbf{k},\quad (3)$$

where  $\mathbf{k}$  represents the position in Fourier space. Now we can relate the magnetic phase shift directly to the magnetization by combining Eqs. (1) and (3) in Fourier space as

$$\phi_m = \frac{i\pi\mu_0}{\phi_0} \frac{|\mathbf{M}(\mathbf{k}) \times \mathbf{k}|_z}{k_\perp^2},\quad (4)$$

where  $k_\perp$  is the position vector in the projection plane in Fourier space, and the subscript  $z$  denotes that we are only keeping the component along the beam direction.

Next we model the total magnetization of an object by dividing it into voxels in real space, each containing a magnetic dipole of uniform magnitude such that the net magnetization is preserved. The magnetic moment for each dipole is given by  $\mathbf{M}(\mathbf{r}) = M_0 [m_x, m_y, m_z]$ , where  $M_0$  is the saturation magnetization and  $m_i$  are the unit-vector components. This lets us rewrite Eq. (4) explicitly in terms of the phase shift resulting from an individual dipole:

$$\phi_{\text{dip}}(k_x, k_y) = m_x S_y - m_y S_x,\quad (5)$$

where  $B_0 = \mu_0 M_0$  is the saturation induction and

$$S_\alpha = \frac{i\pi B_0}{\phi_0 k_\perp^2} k_\alpha, \quad \alpha \in \{x, y\}.\quad (6)$$

Although the magnetization is discretized in real space, the calculation for Eq. (5) is performed in Fourier space, giving us the phase shift from a single dipole. The total phase shift resulting from the object is then given by the sum of the phase shifts for each voxel. This is computed in Fourier space by applying to each phase shift an exponential prefactor related to its real-space position, giving

$$\phi_{\text{obj}}(k_x, k_y) = \sum_{(i,j,k) \in D} e^{i\mathbf{k}_\perp \cdot \mathbf{r}_{ijk}} (m_x S_y - m_y S_x),\quad (7)$$

where  $(i, j, k)$  are the indices of the voxels within the shape function  $D$  that defines the object, and  $\mathbf{r}_{ijk}$  is the position vector of that voxel.

We now expand this by considering samples that are not lying along the coordinates of our microscope reference. Tilting samples in the LTEM instrument can be invaluable as it provides contrast from out-of-plane magnetization components that would not otherwise interact with the electron beam [23,26]. For example, individual tilted images can be used to identify Néel domain walls or skyrmions and to determine vortex polarity [24], while

full tilt series allow 3D tomographic reconstruction of the magnetic vector potential and magnetic induction [27,28].

Tilting in a transmission electron microscope is possible in two orthogonal directions. We let the sample be tilted (counterclockwise) around its  $x$  axis by angle  $\theta$  and about its  $y$  axis by  $\gamma$ , and then recompute the translation vector  $\mathbf{r}_{ijk}$  and the magnetization vector  $\mathbf{m}$  using standard rotation matrices. This lets us rewrite the total magnetic phase shift as a function of sample tilt angle:

$$\phi_m^\theta(k_x, k_y) = \sum_{(i,j,k) \in D} X_{ijk,\theta}, \quad (8)$$

$$\phi_m^\gamma(k_x, k_y) = \sum_{(i,j,k) \in D} Y_{ijk,\gamma}, \quad (9)$$

where

$$\begin{aligned} X_{ijk,\theta} &= e^{i[k_x i + k_y (j \cos \theta - k \sin \theta)]} \\ &\times [m_{ijk,x} S_y - (m_{ijk,y} \cos \theta - m_{ijk,z} \sin \theta) S_x], \end{aligned} \quad (10)$$

$$\begin{aligned} Y_{ijk,\gamma} &= e^{i[k_x (i \cos \gamma + k \sin \gamma) + k_y j]} \\ &\times [(m_{ijk,x} \cos \gamma - m_{ijk,z} \sin \gamma) S_y - m_{ijk,y} S_x]. \end{aligned} \quad (11)$$

The above computation is performed in Fourier space, and by taking an inverse Fourier transform, we obtain the real-space phase shift across the entire image. These equations provide a forward model to compute the magnetic phase shift of any object as a function of tilt angle by summing the contributions of each voxel. These results are similar to the work by Humphrey *et al.* [29], where, instead of magnetic dipoles, they represent each voxel by a sphere with a corresponding magnetic moment.

Our linear superposition technique can also be used to calculate the electrostatic phase shift  $\phi_e$  concurrently with  $\phi_m$ . This is done by replacing the magnetization terms in Eqs. (10) and (11) with a scalar value for the mean inner potential of the sample. The sums in Eqs. (8) and (9) are then multiplied by the microscope interaction constant  $\pi/\lambda E$  and the electrostatic phase shift is determined. Combining  $\phi_e$  and  $\phi_m$  gives the total electron phase shift with which to simulate LTEM images.

This technique however requires increased computation time as compared to those for calculating the phase shift imparted by 2D magnetization structures. Relatively large array operations must be performed for each voxel and, while components such as the  $S$  arrays can be pre-computed, this leads to a larger computation time per voxel than the Mansuripur method. PyLorentz is written in Python, the advantages of which come in flexibility and easy implementation rather than in efficiency. To counter these difficulties, we employ just-in-time compilation of

the algorithm and parallel processing, which increase the computation speeds to an acceptable level. We find that the phase calculation for a  $128 \times 128 \times 128$  grid takes approximately 250 s on a moderately powerful 8-core laptop. Even with these improvements, the Mansuripur algorithm is much faster and is also implemented in PyLorentz to be used when not tilting the sample.

As a verification of the proposed linear superposition method, we calculate the magnetic phase shift of a Landau domain structure. A magnetic island of dimensions  $(L_x, L_y, L_z)$  with an idealized flux closure structure results in a phase shift given analytically by

$$\phi_m(x, y) = \frac{2\pi B_0 L_z}{\phi_0} \min \begin{cases} L_x - |x| \\ L_y - |y| \end{cases}, \quad (12)$$

where we assume  $90^\circ$  domain walls with zero wall width [30]. The phase shift induced by a  $750 \times 375 \times 20 \text{ nm}^3$  Permalloy island with the magnetization configuration shown in Fig. 2(a) is calculated from both the analytical expression and from our linear superposition methods and is shown in Figs. 2(b) and 2(c). Figure 2(d) shows a line profile of the analytical solution, the linear superposition output, and the Mansuripur algorithm phase shifts across the position of the dashed line in (b): as can be seen, all three are equivalent.

We also simulate here the phase shift from a uniformly thick film containing a Néel skyrmion, which is a topologically protected spin texture that can occur in films with out-of-plane magnetization. Néel skyrmions are characterized by the magnetization pointing radially in or out while transitioning from out-of-plane in one direction in the skyrmion core to the opposite out-of-plane direction at the edge of the skyrmion as shown in Fig. 2(e). When imaged in the plane of the microscope, a Néel skyrmion does not induce a phase shift and is therefore not visible. Figure 2(f) shows how tilting the sample, in this case  $30^\circ$  clockwise around the  $x$  axis, allows the skyrmion core to induce a nonzero phase shift that renders it visible in the microscope.

## B. LTEM image simulation

With the phase shift of the electron wave function through the sample now calculated, we can define a microscope and simulate the resulting LTEM images. Here we outline the relevant microscope parameters and demonstrate some of their effects. For a more detailed description of how images are simulated, refer to the appendix.

Figure 3 shows simulated LTEM images with different imaging conditions for the single Néel skyrmion shown in Figs. 2(e) and 2(f). The simulated region is  $320 \times 320 \times 180 \text{ nm}^3$ , calculated with a  $5 \times 5 \times 5 \text{ nm}^3$  cell size. Image (a) is simulated for a 200-kV microscope with the following parameters: defocus  $\Delta z = -25 \mu\text{m}$ , beam divergence

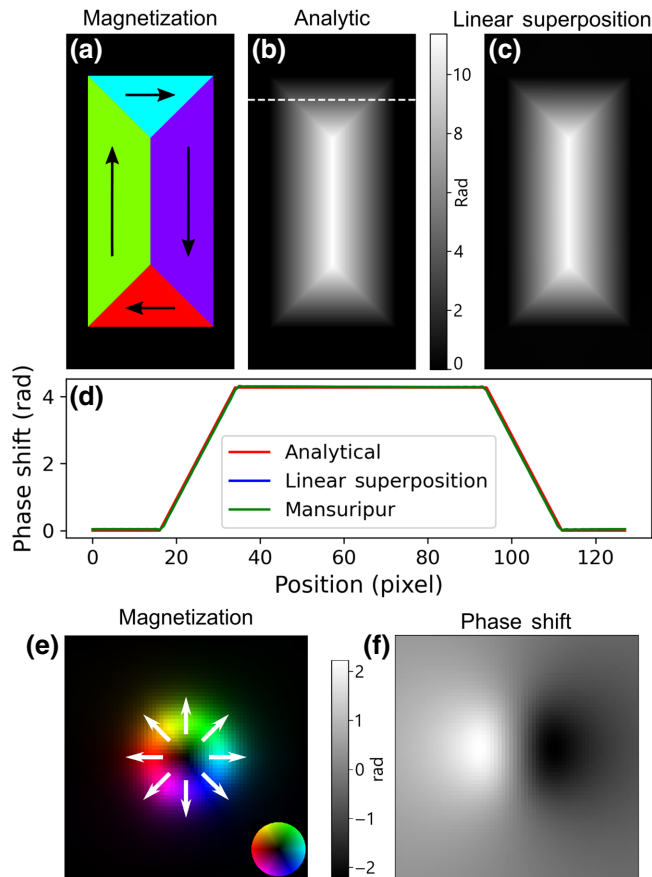


FIG. 2. Magnetic phase shift calculations for a flux closure domain and a Néel skyrmion. (a) A Landau structure in a  $750 \times 375 \times 20 \text{ nm}^3$  Permalloy island. (b),(c) The phase shift calculated from the analytical expression and the linear superposition method, respectively, with a shared scalebar. (d) Line profile of the phase shift across the dashed line in (b) as calculated by the analytical equation, linear superposition method, and Mansuripur algorithm (not pictured). (e) The magnetization of a Néel skyrmion and (f) the corresponding phase shift when rotated  $-30^\circ$  around the  $x$  axis, calculated with the linear superposition method.

$\theta_c = 10 \mu\text{rad}$ , no astigmatism or spherical aberration, and with the sample lying parallel to the  $x$ - $y$  plane. The simulated images have no sources of noise that would occur in experimental data, and as such the defocus value for most simulated images is chosen to be at the low end of practical values. This ensures that the image is calculated well within the small defocus limit [31]. As mentioned earlier, a Néel skyrmion does not generate contrast when viewed in the plane of the microscope, but does when tilted, as seen in (b) and (c), where the sample is rotated  $30^\circ$  and  $60^\circ$  clockwise around the  $x$  axis.

Image (c) shows an asymmetry between the top and bottom edges of the skyrmion, because the magnetization is more out of plane and the demagnetizing field is greater on the bottom edge of the sample due to the Halbach effect

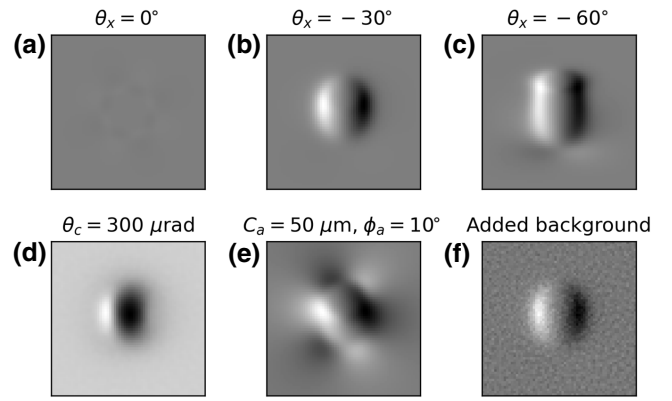


FIG. 3. Simulated LTEM images of a Néel skyrmion with different microscope parameters. All images, unless otherwise specified, are simulated for a  $320 \times 320 \text{ nm}^2$  region with the sample rotated  $30^\circ$  around the  $x$  axis, and with the following microscope parameters:  $\Delta z = -25 \mu\text{m}$ ,  $\theta_c = 10 \mu\text{rad}$ ,  $C_a = 0$ ,  $C_s = 0$ . (a) No contrast is observed when the sample is flat in the  $x$ - $y$  plane with  $\theta_x = 0^\circ$ . (b) When rotated around the  $x$  axis to  $\theta_x = -30^\circ$  and (c)  $\theta_x = -60^\circ$ , the in-plane component of the core makes the skyrmion visible. The spin texture is not as recognizable when (d) decreasing microscope coherence to  $\theta_c = 300 \mu\text{rad}$  or (e) introducing astigmatism  $C_a = 50 \mu\text{m}$  with  $\phi_a = 10^\circ$ . (f) The same imaging conditions as (b), but with an additional random phase shift added to simulate the effects of the support membrane.

[32]. We only observe this due to the higher tilt angle, and because we treat the skyrmion as a 3D spin structure when calculating the phase shift. Even a Néel skyrmion, a texture normally treated as two dimensional, can display variations in the magnetization through the film [33]. This detail would be missed using other phase calculation techniques but is accurately accounted for by the linear superposition method.

In Figs. 3(d)–3(f) the imaging conditions are the same as for (b) except that one parameter is changed. When exploring unconventional spin textures, one must consider whether they will produce visible contrast in the microscope and if that contrast will be sufficient to identify the spin texture. LTEM image simulation therefore plays a role in guiding the experiment. In Fig. 3(d) the relevance of beam coherence in LTEM imaging is highlighted: if we increase  $\theta_c$  to  $300 \mu\text{rad}$ , the visible magnetic contrast is distorted and reduced. Image (e) demonstrates the care that must be taken when interpreting magnetic contrast in the presence of objective lens aberrations. When twofold astigmatism is introduced such that  $C_a = 100 \mu\text{m}$  at an angle of  $\phi_a = 10^\circ$ , we see that the contrast completely changes. This seemingly implies a very different magnetic structure and highlights the usefulness of careful imaging and of verifying experimental observations with simulations.

Lastly, Fig. 3(f) shows an image simulated with the same microscope parameters as (b), but with the addition of a randomly varying phase term to account for the amorphous structure of the support membrane. A randomly varying phase shift applied to each pixel has been shown to accurately model the effects of an amorphous film [34], and the addition of this term is useful as Fig. 3(f) more accurately reflects what an experimental image would look like.

As these examples are for a sample of uniform thickness, changing defocus primarily adjusts the magnitude of the magnetic contrast. For samples with variable thickness, such as the island structure shown in Fig. 2, higher defocus or beam coherence will also increase the Fresnel fringes at the island edges, which can make the image more difficult to interpret.

### C. Mapping Néel skyrmion spin textures

In this section we use PyLorentz to explore simulated and experimental data for Néel skyrmions. We compare the magnetization and stray field produced by a skyrmion lattice to the TIE-reconstructed integrated induction maps.

We begin with a Mumax simulation of Néel skyrmions in a  $640 \times 640 \times 160 \text{ nm}^3$  region of film. The skyrmion cores for the configuration shown in Fig. 4 point into the page (negative  $z$  direction), and the magnetization of the surrounding material points out in the positive  $z$  direction. The following simulation parameters are used:  $5 \times 5 \text{ nm}^3$  cell size, saturation magnetization  $M_0 = 2.2 \times 10^5 \text{ A/m}$ , exchange constant  $A_{\text{ex}} = 10 \times 10^{-12} \text{ J/m}$ , first-order uniaxial anisotropy constant  $K_u = 1.5 \times 10^6 \text{ J/m}^3$ , interfacial DMI strength  $D_{\text{ind}} = 8 \times 10^{-4} \text{ J/m}^2$ , and an applied field  $B = 0.22 \text{ T}$  in the positive  $z$  direction. The magnetic parameters used for these simulations are representative of metallic multilayers, which display skyrmions, but they are tuned such that a relatively sparse skyrmion lattice is produced. As such, while the parameters used are experimentally feasible, these simulations do not correspond to a specific material.

As previously shown, samples containing Néel skyrmions or domain walls must be tilted relative to the electron beam to be visible using LTEM. Figure 4(a) shows a 2D projection of the magnetization after the sample has been rotated  $30^\circ$  clockwise around the  $x$  axis. All of the image simulations and reconstructions shown in Figs. 4(b)–4(f) are performed at the same tilt angle, although it should be noted that the tilted magnetization vectors are not then plugged into the phase-shift calculation, but rather the tilt is accounted for in the linear superposition algorithm as described above. The phase shift is calculated using the linear superposition method and a simulated LTEM image with  $\Delta z = -25 \mu\text{m}$  is shown in Fig. 4(b).

To better interpret the LTEM image, we reconstruct the electron phase shift using the TIE method [35]. The

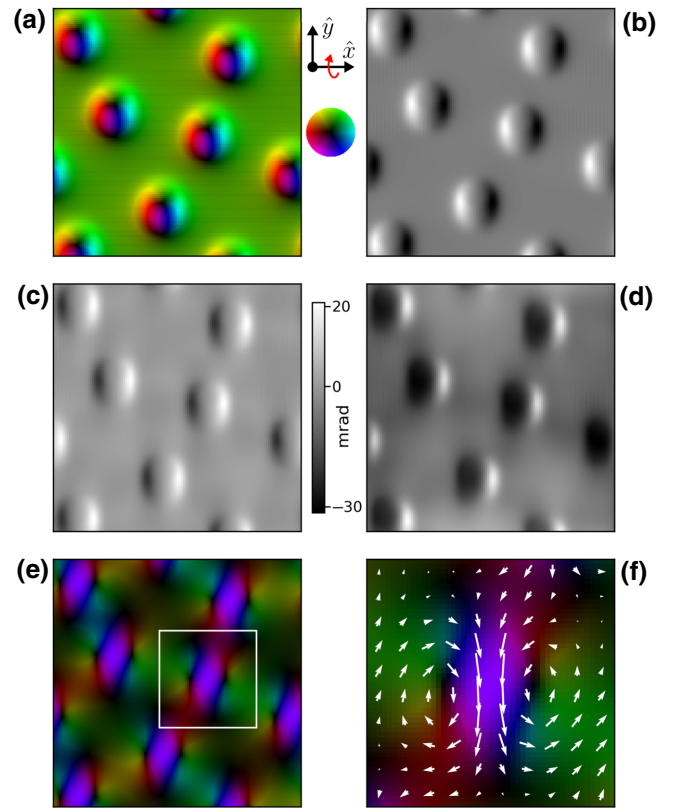


FIG. 4. LTEM image simulations of a  $640 \times 640 \text{ nm}^2$  region containing Néel skyrmions. (a) Relaxed magnetization that has been tilted clockwise around the  $x$  axis by  $\theta = 30^\circ$ . (b) LTEM image simulated at  $\Delta z = -25 \mu\text{m}$  from phase shifts calculated using the linear superposition method. Reconstructions are performed using either a through-focal series and the TIE approach or using the SITIE approach. The difference maps for the magnetic phase shift ( $\phi_m - \phi_{m,\text{TIE}}$ ) and ( $\phi_m - \phi_{m,\text{SITIE}}$ ) are shown in (c),(d) with a common scalebar. The phase shift calculated using the SITIE approach is used to calculate the integrated magnetic induction map shown in (e) with a magnified region (outlined with a white square) shown in (f).

transport-of-intensity equation can be written as

$$\nabla \cdot [I_0 \nabla \phi_t] = -\frac{2\pi}{\lambda} \frac{\partial I}{\partial z}, \quad (13)$$

where  $I_0$  is the in-focus image intensity,  $\lambda$  is the electron wavelength,  $\partial I / \partial z$  is the through-focal image intensity derivative, with  $z$  being along the propagation direction of the electrons, and  $\phi_t$  is the total phase shift. In situations such as this where the electrostatic component of the phase shift is uniform, i.e., the sample is of constant thickness, any variations in  $\phi_t$  will arise from variations in  $\phi_m$ . The TIE formalism cannot determine a uniform offset of the phase, so in this case  $\phi_t$  will represent effectively  $\phi_m$  and the magnetic induction map can be calculated directly by computing the gradient.

For samples with varying thickness, like the Permalloy island seen in Fig. 2(a), the magnetic induction map generated from the total phase shift will lead to an apparent additional field at any change in thickness because of the change in  $\phi_e$ . This problem can be avoided by taking a second through-focal series with the sample inverted in the microscope. The total phase shift for this inverted through-focal series is  $\phi_{i,t} = \phi_e - \phi_m$ . If  $\phi_{i,t}$  and  $\phi_t$  are added or subtracted, the contributions of  $\phi_e$  and  $\phi_m$ , respectively, can be separately obtained. The TIE can then be applied to these phase shifts independently as described in Humphrey *et al.* [36], and this method is included in PyLorentz. Along with making visualization easier, TIE reconstruction also makes possible higher-resolution imaging, as lower defocus is required for reconstruction than for visual interpretation with the naked eye.

As the sample considered here is of uniform thickness, the electrostatic phase shift is uniform and the magnetic induction maps can be reconstructed using the TIE method with only one through-focal series. Additionally, the only source of contrast is magnetic, which allows for a single-image-TIE (SITIE) approach to be used. The in-focus image is approximated as having uniform intensity, leading to a phase reconstructed image without the need for image alignment [21]. Difference maps between the calculated and reconstructed phase shifts for the two approaches ( $\phi_m - \phi_{m,\text{TIE}}$ ) and ( $\phi_m - \phi_{m,\text{SITIE}}$ ), are shown in Figs. 4(c) and 4(d), respectively. The root-mean-squared errors are 5.3 mrad and 11.6 mrad, respectively, which are small compared to the 3.97 rad total phase shift. This demonstrates an accurate reconstruction for both methods with an unsurprising increase in variation when only one single image is used for the SITIE approach. Under experimental conditions, the SITIE method is limited by other image features such as grains in the film, contrast from the support membrane, contamination, and thickness variations.

Figure 4(e) shows the integrated magnetic induction map reconstructed using the SITIE approach, with a magnified region shown in (f). The magnetic configuration seen in (e) resembles a lattice of features that have been referred to as “biskyrmions” or “bound-pair skyrmions” [37–41] and one must take care not to misinterpret the image. The purple regions in which the magnetization points in the negative  $y$  direction correspond to the Néel skyrmion cores with magnetization that pointed into the page (negative  $z$  direction) seen in (a).

Néel skyrmions provide an example of the difference in what is seen between the magnetization, the integrated magnetic induction, and what we observe from a TIE reconstruction. When performing the Mumax simulations, the sample is enclosed within a 1- $\mu\text{m}$  tall region of vacuum vertically surrounding the sample, within which the stray field is also calculated. The magnetic field,  $\mathbf{H}$ , is shown in Fig. 5(a), tilted by  $30^\circ$  around the  $x$  axis like the simulation shown in Fig. 4(a). As  $\mathbf{B} = \mu_0(\mathbf{M} + \mathbf{H})$  we

combine these two vector fields to obtain the tilted integrated magnetic induction shown in Fig. 5(b). The demagnetizing and stray fields hide much of the in-plane component of magnetization in the skyrmions. We see primarily a component of the magnetization at the skyrmion core, now pointing in the negative  $y$  direction, and a component of the out-of-plane magnetization from the surrounding film, which points along the positive  $y$  direction.

The integrated magnetic induction seen in Fig. 5(b) does not exactly match the reconstructed induction seen in Fig. 4(e). The difference is a uniform offset in the  $y$  direction and the result of limitations of LTEM and phase retrieval.  $\mathbf{B}$  fields that are uniform across the field of view are invisible in LTEM images [14]. The TIE method, therefore, can only quantify relative changes in the magnetic induction, but not the absolute value. If one adds a uniform component of magnetic induction to all magnetic vectors seen in Fig. 5(b) such that the  $y$  components across the image sum to zero,  $\sum_{i,j} B_{y,i,j} = 0$ , we obtain the image shown in Fig. 5(c), which matches very well to the TIE-reconstructed magnetic induction. The TIE reconstruction will not be able to determine the uniform offset of the integrated induction as it is not visible in the LTEM image itself. The total field in the  $x$  and  $y$  directions will be due only to contrast visible in the LTEM images, so for a structure with closed loops like the Néel skyrmions the total field in each direction is nearly zero.

The TIE-reconstructed integrated induction, while very useful, can therefore be misleading because it misses uniform components to the magnetic induction that are actually present in the sample. As seen here, the imaged integrated induction can appear very different to the magnetization of the sample, meaning that TIE reconstruction is a technique best used in conjunction with micromagnetic and image simulations. This is especially true when dealing with complex spin structures like skyrmions and situations in which separating out the magnetization is necessary.

Figure 6 shows an experimental LTEM image and reconstruction of Néel skyrmions in a [Pt(1.5 nm)/Co

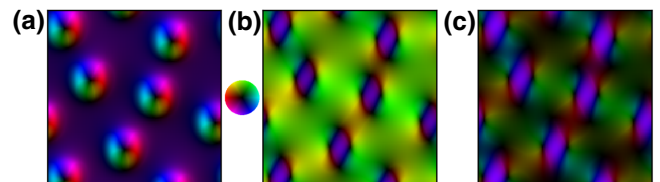


FIG. 5. The effects of stray field. The sample is the same as that shown in Fig. 4, and all images shown are for the sample rotated  $30^\circ$  clockwise around the  $x$  axis with the vector fields summed along the  $z$  direction. (a) The magnetic field  $\mathbf{H}$  calculated in the Mumax simulations. (b) Total magnetic induction  $\mathbf{B} = \mu_0(\mathbf{M} + \mathbf{H})$ . (c) Magnetic induction with a uniform offset applied in the  $y$  direction such that the  $y$  components over the full image sum to 0.

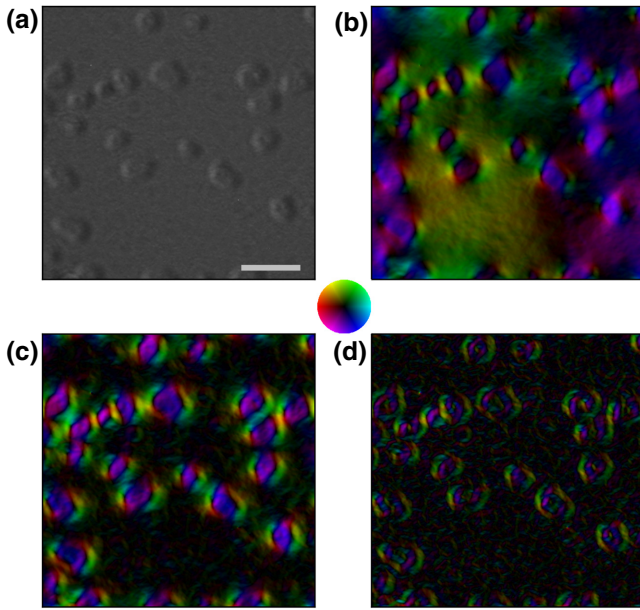


FIG. 6. SITIE reconstruction of an experimental image of a Pt/Co/W multilayer with Néel skyrmions. (a) Underfocus LTEM image with  $\Delta z = -6.4$  mm and  $\theta_x = 30^\circ$ . The scalebar is  $1 \mu\text{m}$ . (b)–(d) SITIE-reconstructed integrated induction (b) without Tikhonov regularization, (c) with  $q_c = 0.0004 \text{ nm}^{-1}$ , and (d) with  $q_c = 0.0017 \text{ nm}^{-1}$ .

(1 nm)/W(1 nm) $^8$  multilayer film. The LTEM image in Fig. 6(a) is recorded with the sample tilted  $30^\circ$  around the  $x$  axis and  $\Delta z = -6.4$  mm. For the magnetic contrast to be visible, a much higher defocus must often be used for experimental data compared to that needed for simulated images, as simulations generally do not include the effects of sample imperfections, contamination, or other sources of noise.

For experimental data, PyLorentz includes several additional features that can improve the quality of phase reconstructions. Whether reconstructing with one through focal series or two, the TIE is solved using an inverse Laplacian method [14]. This allows PyLorentz to implement Tikhonov regularization by modifying the Fourier space kernel of the inverse Laplacian:

$$\frac{1}{q^2} \rightarrow \frac{q^2}{(q^2 + q_c^2)^2}, \quad (14)$$

with  $q_c$  as the Tikhonov frequency. This removes the numerical singularity at the origin and introduces a high-pass filter, which can be used to remove nonmagnetic sources of contrast. Significant care must be taken when picking a  $q_c$  value if the quantitative nature of the reconstruction is to be retained [42,43].

A Tikhonov filter can significantly reduce low-frequency noise, especially when imaging over a larger field of view, but it can also remove or modify real features

and lead to misinterpreting the data. Figures 6(b)–6(d) show the image in (a) reconstructed with the SITIE method using three different values of  $q_c$ . Figure 6(b) shows the integrated induction solved without a Tikhonov filter, i.e.,  $q_c = 0$ . The skyrmion features are difficult to distinguish from a slowly varying background field that results from intensity changes that are not due to magnetic contrast. Figure 6(c) shows the induction reconstructed with  $q_c = 0.0004 \text{ nm}^{-1}$ . The low-frequency background noise is effectively removed without distorting the Néel skyrmion features. The isolated skyrmions in this image match well to the simulated data from Fig. 4, though the image is more difficult to interpret in regions where the skyrmions are packed closely together. Using a high Tikhonov frequency will filter real features from the image, as seen in Fig. 6(d) where the reconstruction is performed with  $q_c = 0.0017 \text{ nm}^{-1}$ .

It is frequently required for LTEM images to be taken well outside the small defocus limit [44,45], and special care must be taken when applying a Tikhonov filter in these cases. A large defocus,  $\Delta z \gtrsim 1$  mm is often used when there is weak magnetic contrast arising due to thin magnetic layers, a small magnetic moment, or viewing out-of-plane magnetic domains at a low tilt angle. Using a Tikhonov filter in these situations can lead to features appearing that are not immediately recognizable as artifacts.

Figure 7 shows LTEM image simulations of a 300-nm skyrmion imaged with increasing defocus and reconstructed with increasing  $q_c$  values. The magnitude of the magnetic contrast increases with defocus, but this is not immediately apparent as each LTEM image in the first column is normalized. Note that the skyrmion appears asymmetric in the LTEM images where  $\Delta z > 1$  mm; this is due to varying interference effects produced by electron waves with positive and negative curvature, which result from positive and negative phase shifts, respectively. This is not due to any asymmetry in the magnetization and is not present in the reconstructed images as the integrated induction is symmetric.

The third and fourth columns of Fig. 7 show how  $q_c$  values of  $0.0005$  and  $0.001 \text{ nm}^{-1}$  can enhance the magnetic contrast of the reconstructed image. These images appear qualitatively similar to the images reconstructed without a filter, and therefore are good representations of the actual magnetic induction. The apparent size of the reconstructed skyrmion increases at larger defocus, and filtering reduces this somewhat. Applying a Tikhonov filter that is clearly too large, in this case  $q_c = 0.004 \text{ nm}^{-1}$ , changes the qualitative shape of the skyrmion and creates a reconstructed image with clear artifacts.

Some  $q_c$  values can lead to artifacts that are not immediately recognizable, however, or that can even appear as plausible magnetic features when imaging well beyond the small defocus limit. In Fig. 7 we see that for  $q_c =$



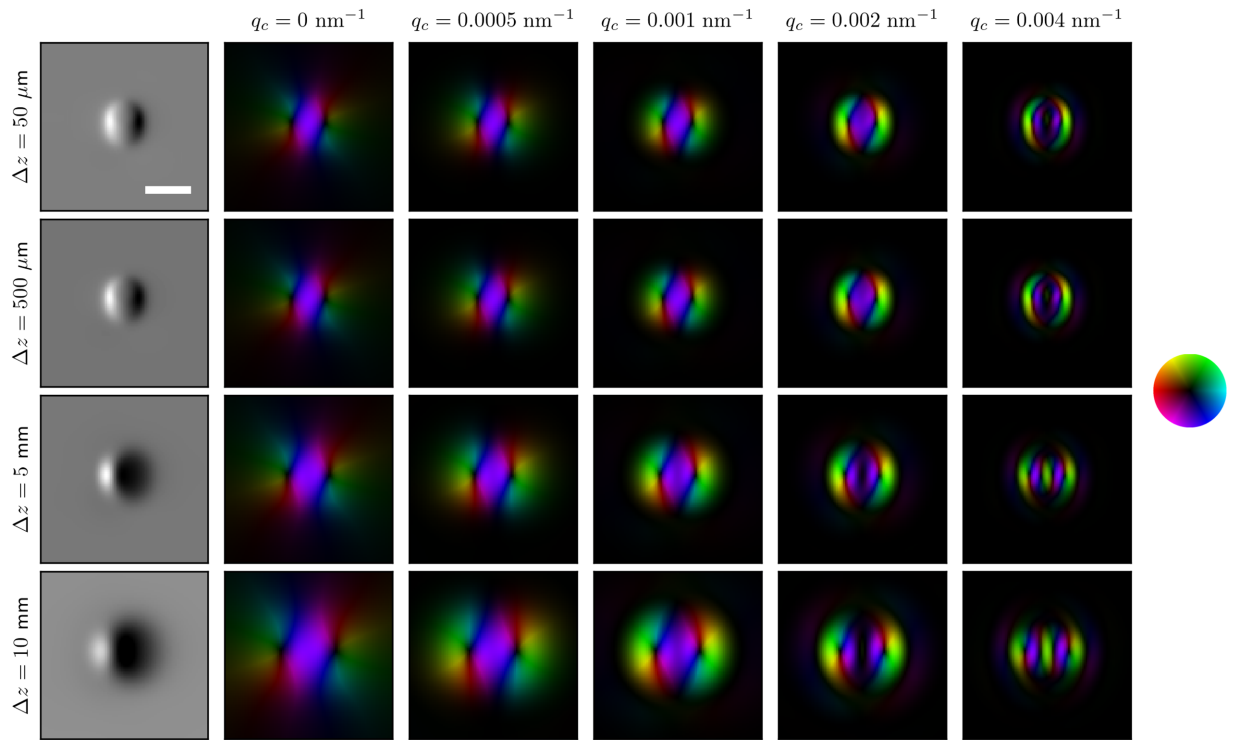


FIG. 7. LTEM images and TIE reconstructions of a Néel skyrmion across a range of defocus values and Tikhonov frequencies. The scalebar is 300 nm, and all images share the same field of view.

$0.002 \text{ nm}^{-1}$  and  $\Delta z = 10 \text{ mm}$ , the skyrmion appears as two distinct magnetic vortices that are clearly separated from each other. This example highlights that care must be taken when interpreting TIE reconstructions; the reconstructed integrated induction can appear physically viable while not at all representing the magnetization of the sample. A range of  $q_c$  values should be tested, and the smallest viable filter should be used to avoid artifacts. Appropriate  $q_c$  values are determined by the feature size, amount of low-frequency noise, tilt angle, and defocus of the image [46].

Filtering can often be avoided by reconstructing a smaller region of interest. A Tikhonov filter can be used to reconstruct full images for qualitative analysis before cropping around a particular magnetic feature. This smaller region of an image, chosen such that bend contours and thickness changes are minimized, can often be reconstructed without filtering to allow for an easy quantitative reconstruction.

### III. DISCUSSION

LTEM is a powerful tool for imaging magnetic spin textures at the nanoscale and is widely used for analyzing skyrmionic materials. TIE reconstruction is a useful technique that enables quantitative maps of the magnetic induction to be reconstructed from the LTEM data, but it is necessary to recognize its limitations. The magnetization,

TIE-reconstructed integrated induction, and actual integrated induction can look very different, though this clarification is often not explicitly stated in the literature. This is partly because the examples provided when discussing TIE reconstruction and LTEM techniques are often flux-closure domains or uniformly magnetized bars with in-plane magnetization. In these cases the distinction is not critical; the limited stray field means that the integrated induction will nearly match the magnetization, and the lack of any uniform field across the image means that the TIE reconstruction will match the total integrated induction. However, for complex spin textures that are of widespread interest, including skyrmions, the distinction becomes relevant. All three fields are different, and one has to be careful of uniform offsets that do not create contrast in the LTEM images and therefore do not appear in the TIE-reconstructed integrated induction.

One example of this can be seen in the literature regarding biskyrmions. Several papers have reported experimental observations of biskyrmions using LTEM [39–41], which has fostered interest in the magnetic texture despite its lack of appearance in micromagnetic simulations. Recent papers by Loudon *et al.* and Yao *et al.* have shown how biskyrmion features can appear when viewing topologically trivial bubble domains at an angle tilted from their symmetry axis [37,38]. Lacking other forms of experimental or simulated evidence for the existence of biskyrmions, the authors conclude that they are best

understood without claiming them to be new magnetic states. This illustrates the kind of mistake that can occur when working with complex spin structures if the TIE reconstructed magnetic induction is interpreted as the magnetization. As seen here in Figs. 4 and 5, the demagnetizing and stray fields cause the TIE reconstruction of even a tilted Néel skyrmion to also appear almost identical to the reported biskyrmions.

To prevent these kinds of errors in the future, micromagnetic simulations and the accompanying simulated LTEM images should be combined with experimental data to better understand complex magnetic features. Without simulations (or additional techniques such as vector field electron tomography) it is not possible to determine the magnetization or gain a complete understanding of the magnetic state of the sample.

To this aim, PyLorentz is an open-source software suite designed to make quantitative analysis of LTEM images easier and more precise. It is built on an algorithm for calculating the complete electron phase shift without restrictions on sample shape or magnetization configuration, and it easily accepts micromagnetic simulation results as an input. LTEM images can then be simulated for varying microscope parameters and imaging conditions, allowing one to test the viability of observing predicted features or compare directly to experimental data. PyLorentz is intended to streamline the process of experimental validation with micromagnetic simulation.

The software is packaged on GitHub and ready to be downloaded and run from Jupyter notebooks, including template files and example data. There is also a graphical user interface (GUI), which contains the TIE functionality without requiring any Python experience.

Image alignment is a useful part of preparing experimental data for TIE reconstruction, and this step is not included in PyLorentz due to the proprietary or patented nature of many leading algorithms. We instead refer users to FIJI [47], which includes several plugins for image registration [48,49]. Even without automated registration, the SITIE implementation of PyLorentz makes at-the-microscope image reconstruction feasible for appropriate samples, including many skyrmionic materials that are of particular interest right now. This technique is also applicable to *in situ* experiments or other situations where it is impractical to take a through-focal series.

We demonstrate the differences between the magnetization, integrated induction, and TIE reconstructed images for quantitative analysis of Néel skyrmion lattices. Skyrmions in thin films are often considered 2D spin structures with a uniform magnetization profile through the thickness of the film, but micromagnetic simulations show that this is not always the case. Understanding the subtle features of skyrmions and other magnetic spin textures is a useful step towards being able to control them effectively for use in devices, and this requires experimental

identification of these 3D structures. That necessitates LTEM image simulations, for which the linear superposition method is able to accurately account for the 3D magnetic structure, which other techniques cannot do. This is even more helpful when searching for hopfions and other topological solitons that are fundamentally three dimensional and have not yet been found experimentally. PyLorentz, using TIE image reconstruction and the linear superposition method, makes LTEM a strong choice for identifying complex magnetic states and analyzing magnetic materials.

## ACKNOWLEDGMENTS

This work is supported by the U.S. Department of Energy, Office of Science, Office of Basic Energy Sciences, Materials Sciences and Engineering Division. Use of the Center for Nanoscale Materials, an Office of Science user facility, is supported by the U.S. Department of Energy, Office of Science, Office of Basic Energy Sciences, under Contract No. DE-AC02-06CH11357.

## APPENDIX: LTEM IMAGE SIMULATION

Here we show how LTEM images are calculated from the total electron phase shift through the sample,  $\phi_t$ . We begin by writing the wave function at the exit surface of the sample as

$$\psi(\mathbf{r}_\perp) = a(\mathbf{r}_\perp)e^{i\phi_t(\mathbf{r}_\perp)}, \quad (\text{A1})$$

where  $a(\mathbf{r}_\perp)$  is an amplitude function defined by the sample shape and by its absorption coefficient, and  $\phi_t$  the electron phase shift induced by the sample as calculated previously. Here we do not include detailed electron scattering for calculation of the amplitude, but only the absorption of the electrons, which is given by

$$a(\mathbf{r}_\perp) = e^{-t/\xi_0}, \quad (\text{A2})$$

where  $t$  is the sample thickness in the beam direction, and  $\xi_0$  is the absorption coefficient for the sample material. In order to calculate the resulting image intensity, we propagate this wave function to the exit plane by convolving it with the transfer function of the microscope in the back focal plane and determining the intensity of the wave function,

$$I(\mathbf{r}_\perp) = |\psi(\mathbf{r}_\perp) * \mathcal{T}(\mathbf{r}_\perp)|^2, \quad (\text{A3})$$

where  $\mathcal{F}$  denotes a Fourier transform,  $*$  is a convolution operation, and  $\mathcal{T}(\mathbf{r}_\perp)$  is the microscope transfer function. This operation is written here in real space but is computed in Fourier space. The TEM transfer function is composed

of three parts [50]:

$$\mathcal{T}(\mathbf{k}_\perp) = A(\mathbf{k}_\perp) e^{-i\chi(\mathbf{k}_\perp)} e^{-g(\mathbf{k}_\perp)}, \quad (\text{A4})$$

where  $A(\mathbf{k}_\perp)$  is the objective aperture function,  $e^{-i\chi(\mathbf{k}_\perp)}$  the phase transfer function, and  $e^{-g(\mathbf{k}_\perp)}$  the damping envelope. The aperture is a binary function (1 inside and 0 outside) centered in reciprocal space for the Fresnel imaging mode. We can define the phase-transfer function as

$$\chi(\mathbf{k}_\perp) = \pi\lambda [\Delta z + C_a \cos(2\phi_a)] |k|^2 + \frac{\pi}{2} C_s \lambda^3 |k|^4, \quad (\text{A5})$$

where  $\Delta z$  is the defocus,  $C_a$  and  $\phi_a$  are the magnitude and orientation of the twofold astigmatism, and  $C_s$  is the spherical aberration coefficient.

The damping envelope can be written as

$$g(\mathbf{k}_\perp) = \frac{\pi^2 \theta_c^2}{\lambda^2 u} (C_s \lambda^3 |k|^3 - \Delta z \lambda |k|)^2 + \frac{(\pi \lambda \Delta)^2}{2u} |k|^4, \quad (\text{A6})$$

where  $u = 1 + 2(\pi \theta_c \Delta)^2 |k|^2$ ,  $\theta_c$  is the beam divergence angle, and  $\Delta$  is the defocus spread [14]. With these parameters defined, it is a simple matter to compute the convolution from Eq. (A3) in Fourier space and simulate a LTEM image from the calculated phase shifts and amplitude of the propagating electrons.

- 
- [1] K. Everschor-Sitte, J. Masell, R. M. Reeve, and M. Kläui, Perspective: Magnetic skyrmions—overview of recent progress in an active research field, *J. Appl. Phys.* **124**, 240901 (2018).
- [2] S. H. Skjærø, C. H. Marrows, R. L. Stamps, and L. J. Heyderman, Advances in artificial spin ice, *Nat. Rev. Phys.* **2**, 13 (2020).
- [3] A. Fert, N. Reyren, and V. Cros, Magnetic skyrmions: Advances in physics and potential applications, *Nat. Rev. Mater.* **2**, 17031 (2017).
- [4] I. Dzyaloshinsky, A thermodynamic theory of “weak” ferromagnetism of antiferromagnetics, *J. Phys. Chem. Solids* **4**, 241 (1958).
- [5] T. Moriya, Anisotropic superexchange interaction and weak ferromagnetism, *Phys. Rev.* **120**, 91 (1960).
- [6] M. He, G. Li, Z. Zhu, Y. Zhang, L. Peng, R. Li, J. Li, H. Wei, T. Zhao, X.-G. Zhang, S. Wang, S.-Z. Lin, L. Gu, G. Yu, J. W. Cai, and B.-g. Shen, Evolution of topological skyrmions across the spin reorientation transition in Pt/Co/Ta multilayers, *Phys. Rev. B* **97**, 174419 (2018).
- [7] W. Jiang, G. Chen, K. Liu, J. Zang, S. G. te Velthuis, and A. Hoffmann, Skyrmions in magnetic multilayers, *Phys. Rep.* **704**, 1 (2017).
- [8] F. Zheng, H. Li, S. Wang, D. Song, C. Jin, W. Wei, A. Kovács, J. Zang, M. Tian, Y. Zhang, H. Du, and R. E. Dunin-Borkowski, Direct Imaging of a Zero-Field Target Skyrmion and its Polarity Switch in a Chiral Magnetic Nanodisk, *Phys. Rev. Lett.* **119**, 197205 (2017).
- [9] P. Sutcliffe, Skyrmion Knots in Frustrated Magnets, *Phys. Rev. Lett.* **118**, 247203 (2017), 1705.10966.
- [10] M. M. Yazid, S. H. Olsen, and G. J. Atkinson, MFM study of a sintered Nd-Fe-B Magnet: Analyzing domain structure and measuring defect size in 3-D view, *IEEE Trans. Magn.* **52**, 1 (2016).
- [11] C. Phatak, A. K. Petford-Long, and M. De Graef, Recent advances in lorentz microscopy, *Curr. Opin. Solid State Mater. Sci.* **20**, 107 (2016).
- [12] J. N. Chapman, The investigation of magnetic domain structures in thin foils by electron microscopy, *J. Phys. D. Appl. Phys.* **17**, 623 (1984).
- [13] M. E. Hale, H. W. Fuller, and H. Rubinstein, Magnetic domain observations by electron microscopy, *J. Appl. Phys.* **30**, 789 (1959).
- [14] M. De Graef, *Introduction to Conventional Transmission Electron Microscopy* (Cambridge University Press, Cambridge, UK, 2003).
- [15] D. Gabor, A new microscopic principle, *Nature* **161**, 777 (1948).
- [16] C. Ophus, Four-dimensional scanning transmission electron microscopy (4D-STEM): From scanning nanodiffraction to ptychography and beyond, *Microsc. Microanal.* **25**, 563 (2019).
- [17] A. R. McCray, T. Cote, Y. Li, A. K. Petford-Long, and C. Phatak, PyLorentz, (2021).
- [18] M. Donahue and D. Porter, OOMMF User’s Guide, Version 1.0, Interag. Rep. NISTIR 6376 (1999).
- [19] A. Vansteenkiste, J. Leliaert, M. Dvornik, M. Helsen, F. Garcia-Sanchez, and B. Van Waeyenberge, The design and verification of MuMax3, *AIP Adv.* **4**, 107133 (2014), 1406.7635.
- [20] Y. Aharonov and D. Bohm, Electromagnetic potentials in the quantum theory, *Phys. Rev.* **123**, 1511 (1961).
- [21] J. J. Chess, S. A. Montoya, T. R. Harvey, C. Ophus, S. Couture, V. Lomakin, E. E. Fullerton, and B. J. McMoran, Streamlined approach to mapping the magnetic induction of skyrmionic materials, *Ultramicroscopy* **177**, 78 (2017).
- [22] M. Mansuripur, Computation of electron diffraction patterns in lorentz electron microscopy of thin magnetic films, *J. Appl. Phys.* **69**, 2455 (1991).
- [23] T. Haug, S. Otto, M. Schneider, and J. Zweck, Computer simulation of lorentz electron micrographs of thin magnetic particles, *Ultramicroscopy* **96**, 201 (2003).
- [24] C. Phatak, M. Tanase, A. K. Petford-Long, and M. De Graef, Determination of magnetic vortex polarity from a single lorentz fresnel image, *Ultramicroscopy* **109**, 264 (2009).
- [25] C. Phatak, A. K. Petford-Long, and O. Heinonen, Direct Observation of Unconventional Topological Spin Structure in Coupled Magnetic Discs, *Phys. Rev. Lett.* **108**, 067205 (2012).
- [26] S. D. Pollard, J. A. Garlow, J. Yu, Z. Wang, Y. Zhu, and H. Yang, Observation of stable Néel skyrmions in cobalt/palladium multilayers with Lorentz transmission electron microscopy, *Nat. Commun.* **8**, 14761 (2017).

- [27] C. Phatak, A. K. Petford-Long, and M. De Graef, Three-Dimensional Study of the Vector Potential of Magnetic Structures, *Phys. Rev. Lett.* **104**, 253901 (2010).
- [28] C. Phatak, Y. Liu, E. B. Gulsoy, D. Schmidt, E. Franke-Schubert, and A. Petford-Long, Visualization of the magnetic structure of sculpted three-dimensional cobalt nanospirals, *Nano Lett.* **14**, 759 (2014).
- [29] E. Humphrey and M. De Graef, On the computation of the magnetic phase shift for magnetic nano-particles of arbitrary shape using a spherical projection model, *Ultramicroscopy* **129**, 36 (2013).
- [30] M. Beleggia and Y. Zhu, Electron-optical phase shift of magnetic nanoparticles: I. Basic concepts, *Philos. Mag.* **83**, 1045 (2003).
- [31] M. Beleggia, M. A. Schofield, V. V. Volkov, and Y. Zhu, On the transport of intensity technique for phase retrieval, *Ultramicroscopy* **102**, 37 (2004).
- [32] M. A. Marioni, M. Penedo, M. Baćani, J. Schwenk, and H. J. Hug, Halbach effect at the nanoscale from chiral spin textures, *Nano Lett.* **18**, 2263 (2018).
- [33] S. Schneider, D. Wolf, M. J. Stolt, S. Jin, D. Pohl, B. Rellinghaus, M. Schmidt, B. Büchner, S. T. Goennenwein, K. Nielsch, and A. Lubk, Induction Mapping of the 3D-Modulated Spin Texture of Skyrmions in Thin Helimagnets, *Phys. Rev. Lett.* **120**, 217201 (2018), 1710.08322.
- [34] G. Y. Fan and J. M. Cowley, The simulation of high resolution images of amorphous thin films, *Ultramicroscopy* **21**, 125 (1987).
- [35] A. Barty, D. Paganin, and K. Nugent, in *Magn. Imaging Its Appl. to Mater.*, edited by M. De Graef and Y. Zhu (Academic Press, San Diego, 2001), Chap. 5, p. 137.
- [36] E. Humphrey, C. Phatak, A. Petford-Long, and M. De Graef, Separation of electrostatic and magnetic phase shifts using a modified transport-of-intensity equation, *Ultramicroscopy* **139**, 5 (2014).
- [37] J. C. Loudon, A. C. Twitchett–Harrison, D. Cortés–Ortuño, M. T. Birch, L. A. Turnbull, A. Štefančič, F. Y. Ogrin, E. O. Burgos–Parra, N. Bukin, A. Laurenson, H. Popescu, M. Beg, O. Hovorka, H. Fangohr, P. A. Midgley, G. Balakrishnan, and P. D. Hatton, Do images of biskyrmions show type-II bubbles?, *Adv. Mater.* **31**, 1806598 (2019).
- [38] Y. Yao, B. Ding, J. Cui, X. Shen, Y. Wang, W. Wang, and R. Yu, Magnetic hard nanobubble: A possible magnetization structure behind the bi-skyrmion, *Appl. Phys. Lett.* **114**, 102404 (2019).
- [39] W. Wang, Y. Zhang, G. Xu, L. Peng, B. Ding, Y. Wang, Z. Hou, X. Zhang, X. Li, E. Liu, S. Wang, J. Cai, F. Wang, J. Li, F. Hu, G. Wu, B. Shen, and X. X. Zhang, A centrosymmetric hexagonal magnet with superstable biskyrmion magnetic nanodomains in a wide temperature range of 100–340 K, *Adv. Mater.* **28**, 6887 (2016).
- [40] X. Z. Yu, Y. Tokunaga, Y. Kaneko, W. Z. Zhang, K. Kimoto, Y. Matsui, Y. Taguchi, and Y. Tokura, Biskyrmion states and their current-driven motion in a layered manganite, *Nat. Commun.* **5**, 3198 (2014).
- [41] J. C. T. Lee, J. J. Chess, S. A. Montoya, X. Shi, N. Tamura, S. K. Mishra, P. Fischer, B. J. McMorrnan, S. K. Sinha, E. E. Fullerton, S. D. Kevan, and S. Roy, Synthesizing skyrmion bound pairs in Fe-Gd thin films, *Appl. Phys. Lett.* **109**, 022402 (2016), 1603.07882.
- [42] M. Mitome, K. Ishizuka, and Y. Bando, Quantitativeness of phase measurement by transport of intensity equation, *J. Electron Microsc. (Tokyo)*, **59**, 33 (2010).
- [43] J. A. Garlow, M. Beleggia, S. D. Pollard, H. Yang, and Y. Zhu, Unconventional domain-wall pairs and interacting bloch lines in a dzyaloshinskii-moriya multilayer thin film, *Phys. Rev. B* **102**, 214429 (2020).
- [44] S. Zhang, J. Zhang, Y. Wen, Y. Peng, Z. Qiu, T. Matsumoto, and X. Zhang, Deformation of Néel-type skyrmions revealed by lorentz transmission electron microscopy, *Appl. Phys. Lett.* **116**, 142402 (2020).
- [45] S. McVitie, S. Hughes, K. Fallon, S. McFadzean, D. McGrouther, M. Krajnak, W. Legrand, D. Maccariello, S. Collin, K. Garcia, N. Reyren, V. Cros, A. Fert, K. Zeissler, and C. H. Marrows, A transmission electron microscope study of Néel skyrmion magnetic textures in multilayer thin film systems with large interfacial chiral interaction, *Sci. Rep.* **8**, 5703 (2018).
- [46] J. Cui, Y. Yao, X. Shen, Y. Wang, and R. Yu, Artifacts in magnetic spirals retrieved by transport of intensity equation (TIE), *J. Magn. Magn. Mater.* **454**, 304 (2018).
- [47] J. Schindelin, I. Arganda-Carreras, E. Frise, V. Kaynig, M. Longair, T. Pietzsch, S. Preibisch, C. Rueden, S. Saalfeld, B. Schmid, J.-Y. Tinevez, D. J. White, V. Hartenstein, K. Eliceiri, P. Tomancak, and A. Cardona, Fiji: An open-source platform for biological-image analysis, *Nat. Methods* **9**, 676 (2012).
- [48] I. Arganda-Carreras, C. O. Sorzano, R. Marabini, J. M. Carazo, C. Ortiz-De-Solorzano, and J. Kybic, Consistent and elastic registration of histological sections using vector-spline regularization, *Lect. Notes Comput. Sci. (including Subser. Lect. Notes Artif. Intell. Lect. Notes Bioinformatics)* **4241 LNCS**, 85 (2006).
- [49] D. G. Lowe, Distinctive image features from scale-invariant keypoints, *Int. J. Comput. Vis.* **60**, 91 (2004).
- [50] M. De Graef and Y. Zhu, *Magnetic Imaging and its Application to Materials* (Academic Press, San Diego, USA, 2000), Vol. 36.